C. R. Mecanique 340 (2012) 41–56

Contents lists available at SciVerse ScienceDirect

Comptes Rendus Mecanique

www.sciencedirect.com

Biomimetic flow control

Control of vortex shedding on a circular cylinder using self-adaptive hairy-flaps

Sebastian Kunze *, Christoph Brücker

TU Bergakademie Freiberg, Institut für Mechanik und Fluiddynamik, Lampadiusstrasse 4, 09599 Freiberg, Germany

ARTICLE INFO

Article history:
Available online 30 December 2011

Keywords:
Fluid mechanics
Flow-control
Cylinder wake-flow

ABSTRACT

Experiments on separation control using flexible self-adaptive hairy-flaps are presented herein. The wake-flow behind a circular cylinder is investigated without and with flexible hairy-flaps at the aft-part of the cylinder. Flow dynamics and hair motion were measured by particle image velocimetry and image processing in a range of Reynolds number $5000 < Re < 31\,000$. The experiments and POD analysis show, that the hairy-flaps alter the natural vortex separation cycle in such a way that the vortices do not shed in a zig-zag like arrangement as in the classical von Kármán vortex street but in line in a row with the cylinder wake axis. Thus, the wake-deficit is largely reduced. Furthermore, flow fluctuations are considerably reduced about 42% in streamwise and 35% in transversal direction compared to the reference case without hairy-flaps, too. The condition for this mode change is the lock-in of the vortex shedding with a traveling wave running through the flexible hair bundles in transversal direction at the aft-part of the cylinder. As a consequence, the vortex shedding frequency is increased, the length of the separation bubble is decreased and drag force is decreased, too. The lock-in appears as a jump-like change of the shedding frequency and a jump in the Strouhal–Reynolds number diagram. However, when the characteristic length for the normalized frequency is chosen as the length of the separation bubble instead of the cylinder diameter, the *Str*–*Re* dependence is regular again. This hints on the relevance of the resonator model as proposed by Sigurdson and Roshko (1988) [16] on vortex shedding mechanism when boundary conditions are changed such as in our case, where the hairy-flap bundle imposes a flexible wall with visco-elastic coupling in transversal direction.

1. Introduction

The flow around bluff bodies is one of the most common flows in technical and natural systems and, from these, the flow around a cylinder is the most investigated model-flow. Typical flow characteristics including instabilities, flow separation and vortex-shedding patterns are well documented for a wide range of Reynolds number and cylinder configurations; for a review, see [1]. Therefore, this flow configuration is often used to qualify new active and passive flow control mechanisms. In the following a passive flow control mechanism is presented using flexible self-adaptive hairy-flaps. The work was stimulated by the recent numerical simulation of [2]. They developed a passive flow control method based on beating cilia in a numerical simulation of a cylinder wake flow at $Re = 250$. Based on their theoretical results, they could show that a porous, cilia-like hairy-coating attached on the downstream-side of a circular cylinder may reduce the mean drag force of about 15% and the lift fluctuations of about 40%. For these maximum reductions they identified a coherent transversal-wave

* Corresponding author.
E-mail addresses: sp.kunze@googlemail.com (S. Kunze), bruecker@imfd.tu-freiberg.de (C. Brücker).

1631-0721/$ – see front matter
doi:10.1016/j.crme.2011.11.009

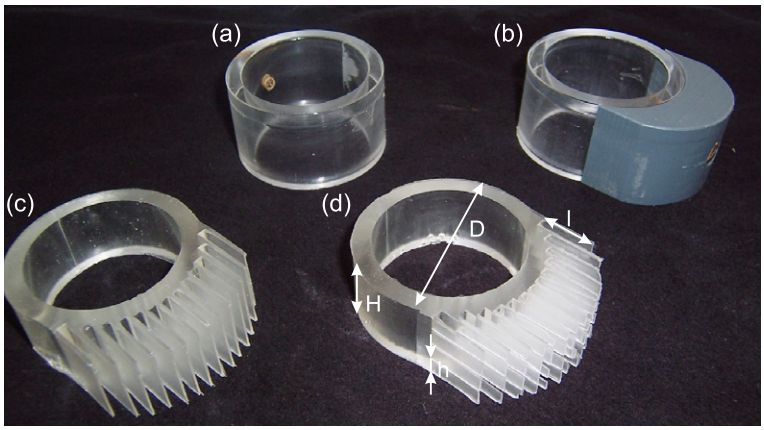

Fig. 1. Classification of test cylinders (only one single segment is shown, the complete cylinder is formed by stacking the total number of 20 segments along the axis): I segment of reference cylinder without hairy flaps; II segment of reference cylinder with attached bluff body; III segment of cylinder with hairy flaps ($h/H = 1$); IV segment of cylinder with hairy flaps ($h/H = 0.1$).

moving through the bundle of cilia, which has a frequency three-time higher than the vortex shedding frequency. Up to now, there is no experimental proof of these effects on cylinder wakes. For cylinders with non-circular cross-section or curved axis, there are numerous studies showing the modification of the separation patterns and, hence the resulting drag and lift forces, too. Experimental investigations on a circular cross-sectional body with a sinuous axis and a circular straight cylinder with hemispherical bumps attached have shown that due to the suppression of vortex shedding, drag reductions up to 47% (body with a sinuous axis) and up to 25% (cylinder with bumps) can be achieved [3–5]. Other studies on cylindrical harbor seal whiskers show that due to their undulated structure the dynamic forces are reduced by at least an order of magnitude, compared to a cylinder with homogeneous cross-section [6]. They showed that this reduction is caused by a changed vortex separation mechanism, which leads to a downstream shift of the vortex formation and a more symmetric pressure field.

Nigim et al. [7] investigated the influence of small circular surface perturbations (diameter d, spacing S) on the drag force and the vortex shedding of a circular cylinder. Their results show that when $S/d < 3$, for d-type arrays [8] the mean value of drag is almost constant and less than that for a smooth-surface cylinder. For these cases, the Strouhal number is higher than that associated with a smooth cylinder. Furthermore, they showed that the effects of surface perturbations on both the mean drag and the vortex-shedding frequency are the result of an apparent shift in the transitional regimes to a lower Reynolds number. Several investigations on the effect of an attached rigid splitter plate on the cylinder wake flow and the dynamics of the forces have been carried out in recent years [9–11]. It is shown, that the length of the splitter plate L strongly influence the character of the vortex shedding for both laminar [10] and turbulent [11] flow. Furthermore, their results show that at critical length $L/D > 1.2$ of the splitter plate the vortex shedding is prevented at all and the net drag is at minimum. Most recent data on a hinged-splitter plate implies that the oscillation of the plate is synchronized to the vortex shedding only in a specific range of Reynolds number [12]. However, force and velocity measurements are still missing and therefore the influence of the motion of the splitter plate on the vortex shedding is unknown up to now. Numerical investigations of Dauptain et al. [13] on beating cilia have shown that beating patterns constituted by long waves oscillating at high frequencies yield very large propulsive velocities which are fed by a blowing effect when the cilia move close to one another. The power output associated with this blowing effect per cilium increases with the frequency as $f^{2.5}$. Furthermore, they showed that the blowing of fluid from the top row is linked with three-dimensional suction on the sides of the cilia. Similar 3D effects of flow around bundles of beating artificial cilia were found by [14].

In the present work a passive flow control mechanism (hairy-flaps), which is inspired by the hairy-coating [2], is developed and investigated experimentally. At first, we describe the geometry of the hairy-flaps and the experimental set-up. Thereafter, the mechanical properties of the hairy-flaps are characterized. Thirdly, we present the experimental results to identify the influence of the hairy-flaps on a cylinder wake flow by the means of velocity distributions, vortex shedding frequencies and proper orthogonal decomposition (POD). Finally, we summarize our findings and present the conclusions of this work.

2. Experimental set-up

The cylinder with the flexible flaps is generated by stacking cylindrical segments with a center bore on a stiff rod, each of the segments cast from silicon rubber as a hollow cylinder with flap-like extensions on the aft part. The two components of the silicon rubber (Wacker RT 601 A and B) were well mixed, vacuumized and filled into the casting form. After the rubber was cured one single element of a hollow cylinder with hairy flaps was extracted from the casting form as a transparent body, see Fig. 1. The thickness of each segment was $H = 20$ mm and the outer diameter $D = 50$ mm. Finally twenty single

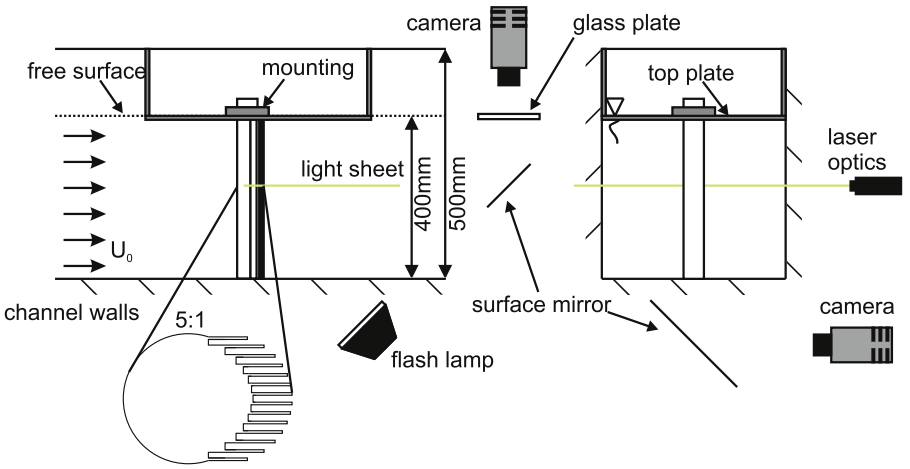

Fig. 2. Sketch of the experimental set-up for the PIV measurements and the determination of the hairy flap kinematics.

segments were stacked over each other on the non-transparent cylindrically rod, resulting in a cylinder with a total height of 400 mm. The ratio of hairy flap length to cylinder diameter and the arrangement of the hairy flaps correspond to the optimum ratio and arrangement found by [2]. The length of one single hairy flap is $l = 0.3$ D and its width $w = 0.05$ D. Two configurations of hairy flap heights h were investigated herein: in the first version each flap has the height of the cylindrical segment with a ratio of $h/H = 1$ (configuration III in Fig. 1); in the second version each element was cut into four smaller hairy flaps $h/H = 0.1$ with a gap of 0.5 mm between each hairy flap (configuration IV in Fig. 1). The second version approximates a more porous situation, where the flow can easily penetrate between the flaps similar to the situation in the numerical investigations of [2]. The flow around the cylinder with hairy flaps was compared to the flow around a reference cylinder without hairy flaps (configuration I in Fig. 1) and a reference cylinder with an attached bluff body (configuration II in Fig. 1). The shape and size of the bluff body is identical to the hull contour of the segments along the flap-tips.

The test cylinders with an outer diameter of $D = 40$ mm and a length of $L = 400$ mm were placed in an open water channel with a cross-section of 400×400 mm^2 and 2D PIV was used to measure the velocity distribution (see Fig. 2). Therefore a laser light sheet (Continuum Minilight II – Nd:YAG Laser, 532 nm) was spanned in the mid-plane of the model and a digital camera (PCO.1600, pixel resolution of 1600×1200 px at a recording frequency of 14 Hz) was used to record the particle image displacements. The orientations of camera and light sheet are shown in Fig. 2. The cylinders were mounted at the top of the water channel. In addition a top plate was placed right under the water surface to achieve approximately a constant bulk velocity profile upstream of the cylinders. The blockage of the channel flow by the cylinder was 10% (projected area of cylinder/channel cross-section). Furthermore, the kinematics of the hairy flaps were determined independently. Therefore, a surface mirror was placed in the water channel downstream of the cylinder at a distance of 24 D, see Fig. 2. The hairy flap-tips were marked black and a flash lamp was used for illumination. A high-speed camera (Photron Fastam RS with a resolution of 1024×1024 px at a recording frequency of 50 Hz), which was synchronized with the flash lamp, was used to record the hairy flaps motion at a recording frequency of 50 Hz. A glass window was used on the free water–air surface to circumvent image distortions due to light reflections on the surface, see Fig. 2.

The dimensions of the field of view for the PIV-measurements was 6×4.16 D. For the calculation of velocity vectors (Dantec Dynamic Studio V3.12) the recorded images were correlated by an adaptive cross-correlation algorithm on a 32×32 px grid with an overlap of 50%. Then a peak validation algorithm was used. The average ratio of valid vectors to calculated vectors was 95.7% and the total amount of vectors per area was 12.21 vectos/cm^2. Thereafter, the velocity vectors were locally smoothed by a moving average filter of 5×5 kernel size. These results are further used for statistical analysis and POD processing. The overall measurement period was $t_{measure} = 24$ s.

2.1. Characterization of mechanical properties

Favier et al. [2] have shown, that the mechanical properties of the hairy flaps have crucial influence on the character of the wake flow behind the cylinder and therefore on the lift and drag force affecting the cylinder. In our case, the density ratio of the hairy flap to the fluid is $m^*_{water} = 1.07$. The fundamental frequency of one single hairy flap was determined by its step response function to a deflection (Fig. 3). The oscillations of the hairy flaps tips were recorded by a high-speed camera (Photron Fastam RS with a resolution of 1024×1024 px at a recording frequency of 500 Hz). Then a feature tracking algorithm was used to calculate the position of the hairy flaps end face in each recorded image. The resulting oscillation of a single hairy flap in water is illustrated in Fig. 4 for both hairy flap configurations ($h/H = 0.1$ and $h/H = 1$). Since the motion of the hairy flap can be described as a damped harmonic oscillator, a damped sine function (Eq. (1)) was fitted on the step response function, with y deflection of the hairy flap-tip, t time, A amplitude, τ relaxation time, ω angular frequency, ϕ phase shift and y_0 offset in y-direction.

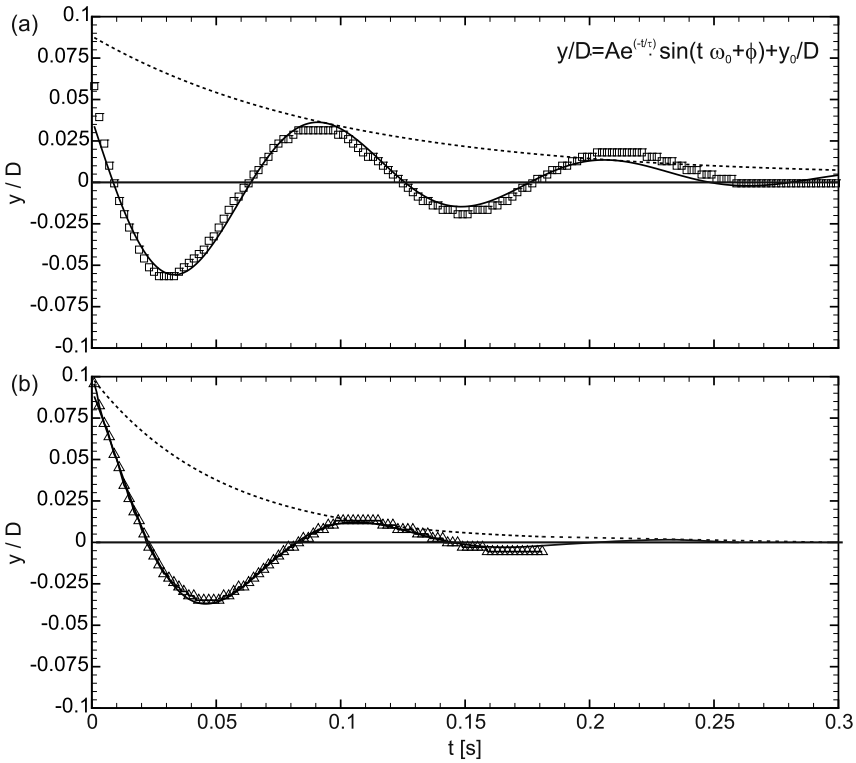

Fig. 3. Step response function of a single hairy flap in water after an arbitrary impulse for aspect ratios (a) $h/H = 0.1$; (b) $h/H = 1$; symbols representing the measured positions of the hairy flap-tip; solid lines representing the fitting function $y/D = Ae^{(-t/\tau)} \cdot \sin(t \cdot \omega_0 + \phi) + y_0/D$ and dashed lines representing the envelope function $y/D = Ae^{(-t/\tau)}$. The positions of the hairy flaps tips y were normalized with the diameter of the cylinder D.

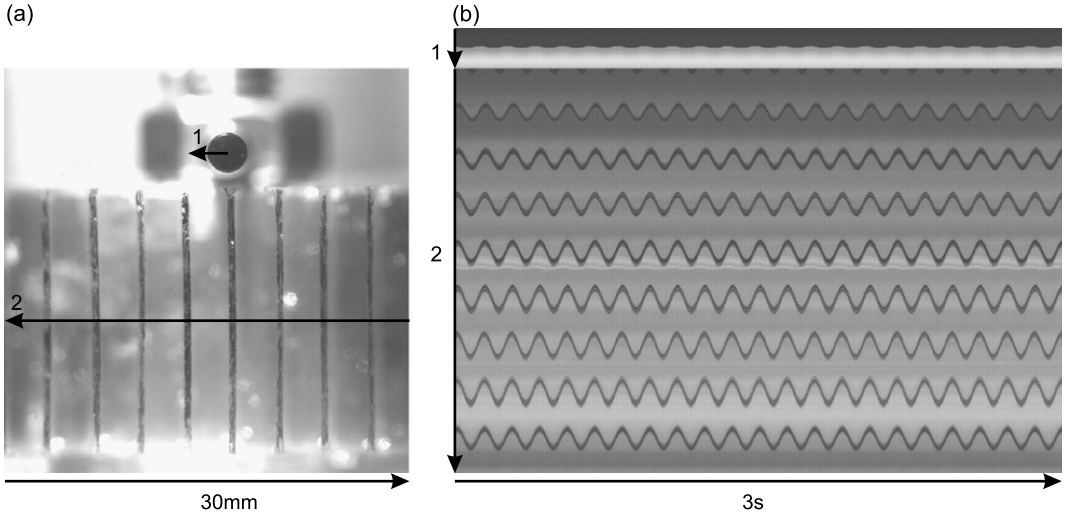

Fig. 4. Illustration of the determination of the impulse response function of the bundle of hairy flaps ($h/H = 1$) at a sinusoidal forcing: (a) example image 1) reference rod and 2) hairy flaps ($h/H = 1$); (b) spatial-temporal reconstruction of hairy flap ($h/H = 1$) movement over 3 s at a forcing frequency of 8.5 Hz.

$$y = f(t) = Ae^{(-t/\tau)} \cdot \sin(t \cdot \omega_0 + \phi) + y_0 \tag{1}$$

In addition, the theoretical fundamental frequency in vacuum is calculated. Both hairy flap-configurations were approximated at first order by a cantilever plate. Therefore, the differential equation for an oscillating beam was used to calculate the fundamental frequency. Neglecting viscous damping of the fluid, normal forces and rotational inertia, the equation of motion for a constant Young's-modulus E, a constant geometrical moment of inertia I and a constant cross-section S of the hairy flap then reads:

Table 1
Summary of the parameters of the curve-fitting algorithm for $y/D = Ae^{(-t/\tau)} \cdot \sin(t \cdot \omega_0 + \phi) + y_0/D$ and theoretical analysis for both height ratios of hairy flap $h/H = 0.1$ and $h/H = 1$. In addition the values of the measured fundamental frequency in water $f_{N,water}$ and of the damping ratio ξ are given.

Parameter	$h/H = 0.1$	$h/H = 1$
ρ_{flap}	1067 kg/m^3	
E	1.57 MPa ... 2.22 MPa	
τ	0.0974 s	0.05095 s
ω_0	54.53 s^{-1}	52.174 s^{-1}
ϕ	0.0441	0.973
$f_{N,water} = 2\pi\omega_0$	8.67 Hz	8.3 Hz
$\xi = 1/(\tau \cdot \omega_0)$	0.188	0.375

$$-EIy'''' = \rho S\ddot{y} \tag{2}$$

The analysis of the eigen-problem of Eq. (2) leads to relation between the fundamental frequency $f_{N,i}$ and the dimensionless wave-number of the ith eigen-mode κ_i (Eq. (3)). In Eq. (3) l is the length of the hairy flaps, w the width of the hairy flaps, ρ_{flap} the density of the silicon rubber and i the number of the eigen-mode:

$$f_{(N,i)} = \frac{(w\kappa_i^2)}{(2\pi l^2)}\sqrt{\frac{E}{12\rho_{flap}}} \tag{3}$$

As seen from Eq. (3) the fundamental frequency $f_{N,i}$ is independent from the height h of the hairy flaps. Therefore, both hairy flaps-configurations $h/H = 1$ and $h/H = 0.1$ have the same fundamental frequency in vacuum. For the first eigen-mode of an oscillating cantilever beam the dimensionless wave-number equals $\kappa_1 = 1.875$. Since the material of the hairy flaps is a silicon rubber the Young's-modulus strongly depend on various factors e.g. temperature, mixing ratio of components A and B and aging and is given in a range between 1.57 MPa and 2.22 MPa. The results of the experimental and theoretical analysis are summarized in Table 1.

The plots in Fig. 3 and Table 1 show, that the damping for the hairy flap with $h/H = 1$ is greater than the damping for the hairy flap with an aspect ratio of $h/H = 0.1$, due to the added mass effect. Therefore, the damping ratio $\xi = 1/(\tau \cdot \omega_0)$ is closer to one (Table 1). At critical damping ξ is equal to one and the step response function converges to that of a critical damped motion without oscillating. Applying a fast Fourier transformation (FFT) on the impulse response function leads to the power spectrum of the oscillation. The global maximum of the power spectrum corresponds to the fundamental frequency of a single hairy flap (Table 1). The experiments were performed 10 times resulting in an ensemble averaged fundamental frequency for the hairy flaps (Table 1). The measured fundamental frequencies $f_{N,water}$ agree well with the angular frequencies ω_0 resulting from the curve-fitting algorithm.

In the bundle of hairy flaps the oscillation of a single hairy flap is influenced by the proximity to the neighboring hairy flaps and the fluid in the gap between two hairy flaps, see [2]. To estimate the influence of these factors on the impulse response function, the whole bundle of hairy flaps was mounted on a rotary oscillator. Then the bundle was activated to oscillate by a sinusoidal small amplitude force with a frequency of $f_{forcing}$. The position of the hairy flaps tips were recorded by a high-speed camera and then tracked in all images. In addition, the position of a stiff reference rod of the same length was tracked in the same way. Fig. 4(a) illustrates a single recording. The hairy flaps tips and the reference rod are marked in black.

Fig. 4(b) shows the spatial-temporal reconstruction of the gray values along the two lines 1 and 2 in Fig. 4(a) over 3 s. The motion of the hairy flaps and the reference rod can be identified by the dark, sinusoidal lines in Fig. 4(b). The amplitude of the reference rod is small compared to the amplitude of the hairy flaps. Furthermore, all hairy flaps were oscillating in nearly the same phase, which is true for all investigated cases. However, one can see a notable phase shift between the motion of the reference rod and the hairy flaps, which increases with increasing forcing frequency. Fig. 5 summarizes the results of the forced oscillation experiments for the second hairy flap from the right-hand side in Fig. 4(a). Since the motions of all hairy flaps are synchronous, the results for this single hairy flap are representative for all hairy flaps in the bundle. In Fig. 5(a) the amplitude distribution of hairy flap ($h/H = 1$) and reference rod for a forcing frequency of 8 Hz and 8.5 Hz over 6 s are shown. The maximum amplitude of the hairy flap at $f_{forcing} = 8.5$ Hz is larger than the maximum amplitude at $f_{forcing} = 8$ Hz, even though the amplitude of the reference rod is nearly identical for the two forcing frequencies. Furthermore, the phase shift between the motion of the reference rod and the hairy flap at $f_{forcing} = 8.5$ Hz is larger than the phase shift at $f_{forcing} = 8$ Hz. The greater phase shift is caused by the greater inertia of the hairy flaps and more importantly the fluid between the hairy flaps at the higher forcing frequency.

Fig. 5(b) compares the maximum values of the amplitude of one hairy flap, the reference rod and the difference between both at increasing forcing frequency. The plot has a clear maximum at $f_{forcing}/f_{N,water} = 1$. Therefore, the natural frequency of the hairy flap is not influenced by the neighboring hairy flaps or the fluid between the hairy flaps, which is in good agreement with the results of [2]. Regarding to the findings of [2], the fundamental frequency of a wave traveling through the bundle of hairy flaps f_N^* is mainly affected by the fundamental frequency of a single hairy flap f_N in the bundle.

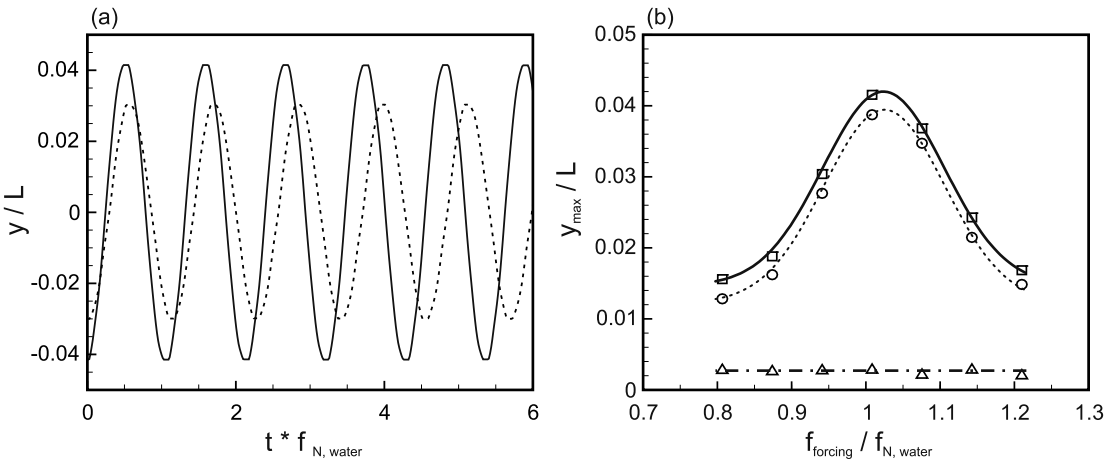

Fig. 5. Results of the forced flap motion: (a) normalized position of one hairy flap-tip ($h/H = 1$) y/L as a function of time t normalized with the fundamental frequency of the hairy flap in water $f_{N,water}$ for a forcing frequency of: --- $f_{forcing} = 8$ Hz; — $f_{forcing} = 8.5$ Hz; (b) dependency of maximum normalized amplitude y_{max}/L from the forcing frequency $f_{forcing}$ normalized with natural frequency in water $f_{N,water}$ for: □ hairy flap-tip ($h/H = 1$); △ tip of the reference rod; ○ difference.

3. Results

All flow measurements were carried out in a range of Reynolds number $5000 < Re < 31\,000$ defined with the mean flow velocity and the diameter of the cylindrical front-part of the bluff body. Fig. 6 displays the time averaged flow field around the four test cylinders at $Re = 27\,750$. The two configurations of hairy flaps ($h/H = 1$, Fig. 6(c); $h/H = 0.1$ Fig. 6(d)) are compared with the reference cylinder without hairy flaps (Fig. 6(a)) and with the reference cylinder with attached bluff body (Fig. 6(b)).

The positions and silhouettes of the test cylinders are indicated in black and all velocity vectors in the shadow region beneath the cylinders are blanked out. As described above, the refractive index of the silicon rubber is approximately the same as water, resulting in the fact that adequate velocity vectors can even be detected in the gap between the hairy flaps. Since the added mass of the smaller hairy flaps $h/H = 0.1$ (Fig. 6(d)) is much smaller than that for the flaps with $h/H = 1$ (Fig. 6(c)), their motion in the wake is much more pronounced at large Re. This motion affects the cross-correlation algorithm of the PIV, resulting in erroneous velocity vectors in Fig. 6(d) at the upper hairy flap ($x/D = 0.3$, $y/D = 0.5$).

The size of the recirculation areas behind both cylinders with movable hairy flaps (Fig. 6(c), (d)) is notably smaller than the size of the recirculation area behind the reference cylinder (Fig. 6(a)). However, behind the reference cylinder with attached bluff body (Fig. 6(b)) no or at least only a very small separation bubble can be identified, since the flow is already in a transitional regime and therefore flow separation is delayed to larger distances downstream from the stagnation point. Comparing Fig. 6(b) with Fig. 6(c) and (d) one can see that even though the size of recirculation area behind the cylinders with hairy flaps are decreased relative to the reference body, however the effect is not as pronounced as for the case in Fig. 6(b).

The differences between time averaged flow field for the reference cylinder and the cylinders with hairy flaps are originated in the influence of the hairy flaps on the vortex shedding. Therefore, the dynamics of the flow is investigated in more detail. In Fig. 7 the flow field for a similar state in the vortex shedding cycle are plotted at different Re numbers ($Re = 12\,062$, $Re = 14\,750$, $Re = 20\,125$) for the reference cylinder and the cylinder with hairy flaps ($h/H = 1$).

In addition, the vorticity distribution ω_z (only the out-of-plane component) with superimposed vector plots are given for a whole period of vortex shedding for the reference cylinder and the cylinder with hairy flaps ($h/H = 1$) at $Re = 20\,125$ in Appendix A (Figs. A.18 and A.19). For the case of the reference cylinder with attached bluff body no clear vortex shedding could be identified. The vector fields for the cylinder with hairy flaps are mirrored at the y-axis for better comparison to the reference case and the cylinder contour is indicated by its silhouette. Only every second vector is displayed in both directions. In addition, Fig. 7 shows the corresponding power spectra of the y-component of U_x calculated at a position of $x/D = 2$, $y/D = 0$, indicated by the black "X" in Fig. 7(a). The global maximum of the power spectra corresponds to the vortex shedding frequency f_S. At low Reynolds number ($Re = 12\,062$), one can see that the character of the vortex shedding and the vortex shedding frequency are similar for both cases, see Fig. 8(a), (b). However, for increasing Reynolds number ($Re = 14\,750$, $Re = 20\,125$) it appears that the transversal location of the vortex being shed from the cylinder is shifted closer towards the centerline ($y/D = 0$) in case of the cylinder with hairy flaps. Similar important is the fact that the vortex shedding frequency for the case with hairy flaps increases, again indicating a change of the character of vortex shedding cycle.

In addition, the root mean square values (rms) of the velocity component U_y in the wake flow were determined. Because of conservation of momentum the fluctuations in the flow affect the fluctuations of lift and drag force. To estimate the

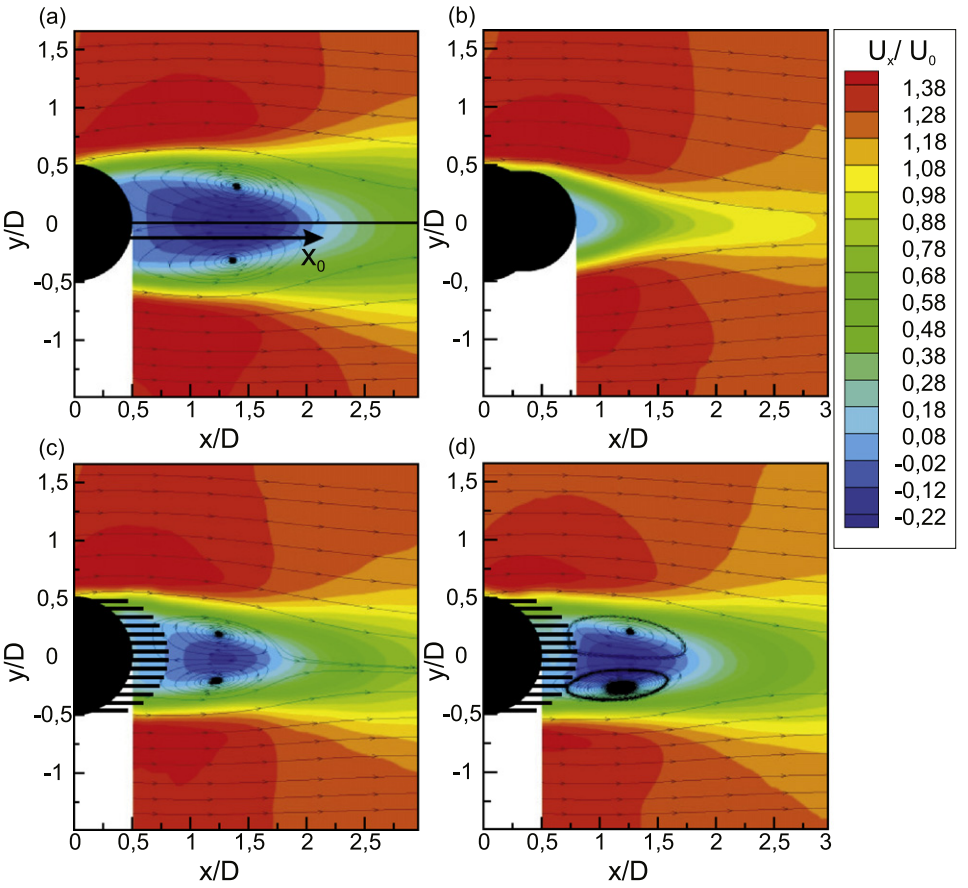

Fig. 6. Contour plot of the time averaged streamwise velocity component U_x normalized with free stream velocity U_0 and sectional streamlines at $Re = 27\,750$ for: (a) reference cylinder without hairy flaps; (b) reference cylinder with attached bluff body; (c) cylinder with hairy flaps, $h/H = 1$; (d) cylinder with hairy flaps $h/H = 0.1$.

intensity of the force fluctuations the region of the separation bubble was determined corresponding to regions of $U_x < 0$ and the rms-values of the velocity vectors in this region were spatially averaged. Therewith, the mean value of rms of the velocity can be used to estimate the qualitative influence of the hairy flaps on force fluctuations. Fig. 9 plots the maximum value of rms(U_y) for the test cylinders with hairy flaps, normalized with the maximum value of rms(U_y) for the reference cylinder. Therefore, values smaller 100% indicate less intense force fluctuations as well. The solid black lines in Fig. 8 illustrate the approximately linear relation between *Re* and vortex shedding frequency predicted by a constant Strouhal number in the investigated range.

The normalized values of vortex shedding frequency for the reference cylinder are in good agreement with the values given in literature for a straight cylinder in cross-flow [1]. The same holds for the hairy flaps for low Reynolds numbers. However, for both hairy flap configurations there is a noticeable jump at $Re \approx 14\,000$ towards higher f_S than the reference case. Even for larger Reynolds number, the Strouhal number remains at the elevated level. Comparing this observation with the trend of rms(U_y) for the different Reynolds numbers, a clear global maximum of rms(U_y) can be found at the critical Reynolds number where the jump appears in f_S. Therefore, the jump in f_S is correlated to a resonance phenomenon between the bundle of hairy flaps and the vortex shedding. It has been argued by [2] that the highest values of rms(U_y) can be found when the vortex shedding frequency is equal to the fundamental frequency of a transversal-wave traveling through the bundle of hairy flaps f_N^*. In their case, the fundamental frequency of the transversal-wave f_N^* is identical to the fundamental frequency of a single hair f_N since the viscous coupling between the hairs is low. In our case the vortex shedding frequency at the position of the jump is ≈ 5 times smaller than the fundamental frequency of the hairy flaps. Herein, it must be taken into account that the viscous coupling between the hairy flaps in our experiments is much larger due to the added mass effect and the squeezing of the flow between the flaps. Therefore, the fundamental frequency of the transversal-wave is assumed to be considerably smaller in our case than the fundamental frequency of a single hairy flap.

To prove our observations of the resonant interaction, the motions of the hairy flaps were recorded by a high-speed camera (Photron Ultima RS). A surface mirror was mounted downstream of the cylinder in such a way to record the end faces of the hairy flaps (Fig. 1). Furthermore, the end faces were marked in black and the cylinder was illuminated by a flash-lamp, synchronized to the camera. Since a glass plate was mounted flush to the free water surface, image distortions

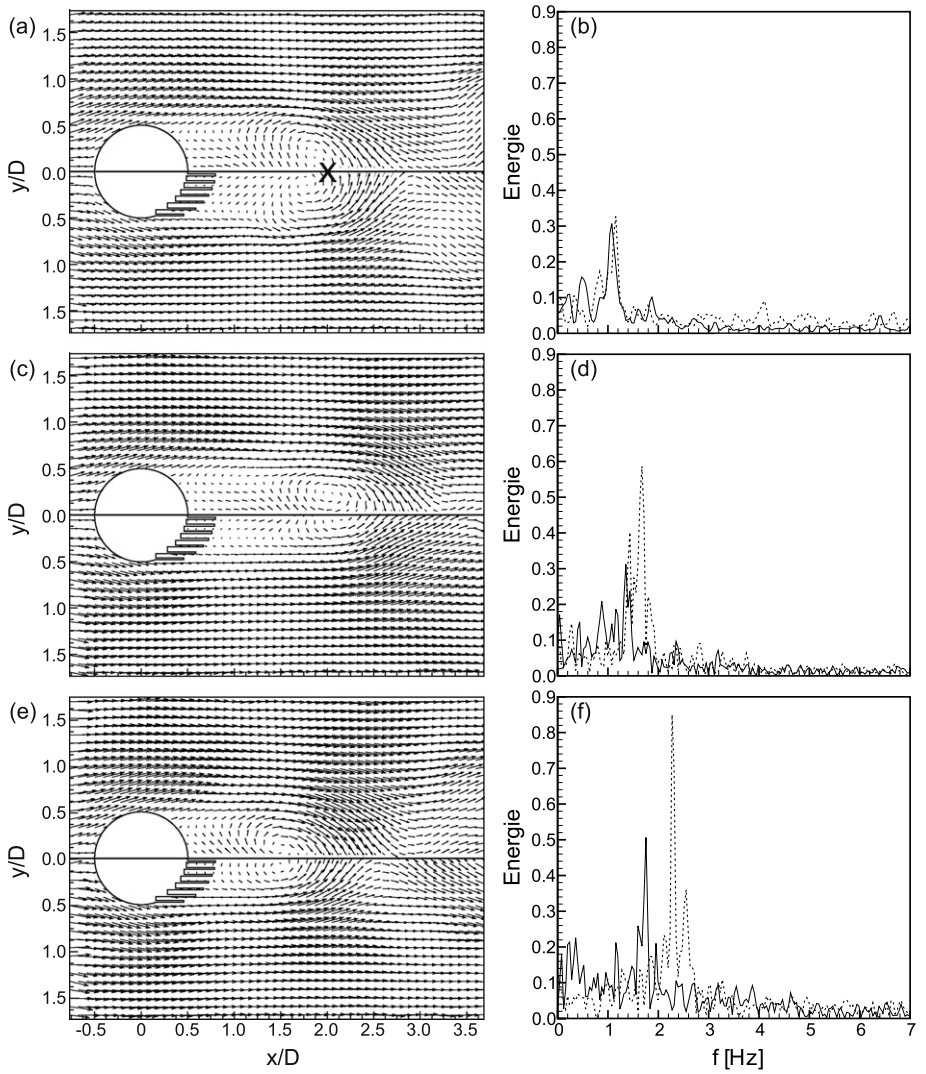

Fig. 7. Comparison of vector plot for a similar instant in the vortex shedding cycle at the reference cylinder and the cylinder with hairy flaps ($h/H = 1$) for: (a) $Re = 12\,062$; (b) $Re = 14\,750$; (c) $Re = 20\,125$. Every second vector in both directions is skipped. In the right column the corresponding power spectra of the velocity component U_y are given for: — reference cylinder; - - - cylinder with hairy flaps ($h/H = 1$). The spectra were calculated at $x/D = 2$, $y/D = 0$ indicated by the black "X" in (a).

due to free water/air surface waves were avoided (Fig. 9). The motions of the hairy flaps were recorded for the same range of *Re*. The positions of the hairy flap-tips in the recordings were calculated over the whole measurement period by a tracking algorithm (Fig. 10). In Fig. 10 the spatial-temporal reconstruction of the gray-values along a horizontal line perpendicular to the main axes of the cylinder is illustrated. Furthermore, the calculated positions of the end faces of the hairy flaps are given in red.

The deflection of the hairy flaps is normalized with the cylinder diameter D and time is normalized with the vortex shedding frequency f_S (Fig. 10). In addition the hairy flaps are numbered for a clear differentiation. The tracking algorithm can reconstruct the hairy flaps motion with sufficient accuracy smaller than $t = 1\%$ of the maximum amplitude. Furthermore, one can identify time domains in which the amplitude of the hairy flap-tips is considerably enhanced and neighboring hairy flaps move synchronous to each other. Some of these domains are marked by red lines connecting local maxima of the hairy flaps-motion (Fig. 10). The motions of the hairy flaps in the marked time domains and their clearly recognizable correlation indicate a wave-like motion through the bundle of hairy flaps in transversal direction. At small *Re*-numbers, all hairy flaps seem to move synchronous, therefore the phase-shift is close to zero (Fig. 10). Hence, the damping of the hairy flaps is only marginal and the influence of the hairy flaps on the wake flow is comparable to that of the bluff body (configuration II in the figure). This indicates at a rather low level of fluid-structure interaction under this conditions. At increasing Re-number the results show an increase in phase-shift between neighboring hairy flaps, indicating a traveling wave-like propagation of the hairy flaps deflection. The wave speed of this transversal wave corresponds to the slope of the red line in Fig. 10(b).

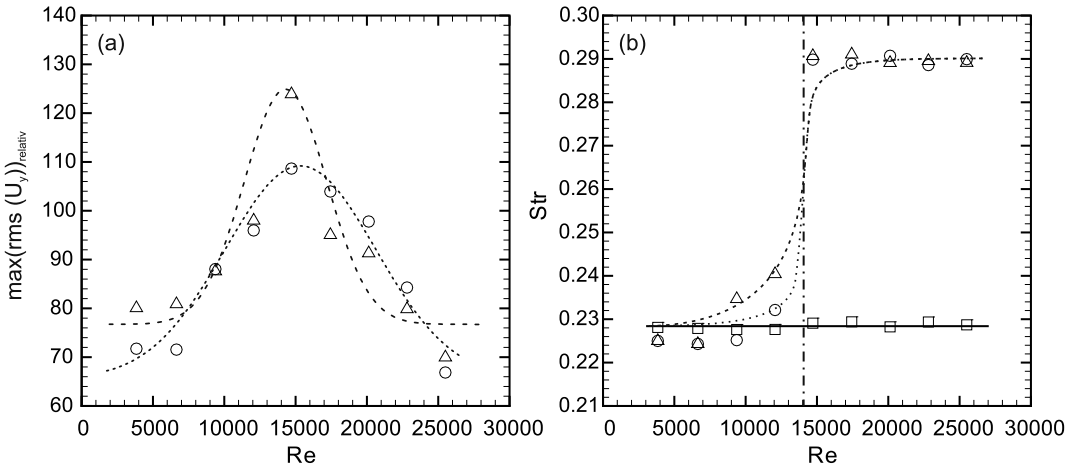

Fig. 8. Plot of (a) dependency of normalized maximum value of rms of velocity component U_y in the wake flow from the Reynolds number for: △ $h/H = 1$ and ○ $h/H = 0.1$; (b) Strouhal number *Str* as a function of Reynolds number *Re* for: □ reference cylinder; △ cylinder with hairy flaps, $h/H = 1$; ○ cylinder with hairy flaps, $h/H = 0.1$.

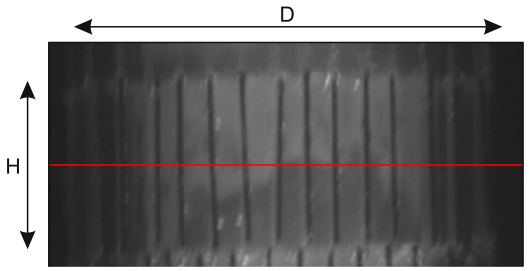

Fig. 9. Image of the hairy flap-tips recorded by the high-speed camera from behind of the cylinder illustrating the instantaneous position of the hairy flap-tips ($h/H = 1$).

The influence of the transversal wave on the wake flow, especially the energy consumption caused by its damping, is visible in the jump of the Strouhal number at the very same Reynolds number ($Re = 14\,750$ in Fig. 8(b)). For higher Re-numbers the wave-speed of the transversal wave is increasing, according to the increased vortex-shedding frequency f_S. Therefore we concluded that the jump in shedding frequency appears at the specific condition, where the shedding frequency for increasing Reynolds number matches to the first time the fundamental frequency of a transversal traveling running over the hairy flaps as a damped oscillator.

Measuring f_N^* in the same way as Favier et al. [2] deduced it from their results is nearly impossible in our case. Instead, we determined the wave speed along the hairs from the temporal shift between the motion of the hairy flap-tips by cross-correlating the reconstructed hairy flap position of the ith hairy flap with that of the fifth hairy flap for the time instants $12, 13, 14 \cdot f_S$ in Fig. 11. Fig. 11 illustrates the relation of the spacing between the i'th and fifth hairy flap $y(i, 5)$ and the calculated time shift $\Delta t(i, 5)$ for $Re = 14\,750$.

The relation between $y(i, 5)$ and $\Delta t(i, 5)$ is approximated by a linear regression, the slope of which corresponds to the wave-speed of the transversal wave. The wave-length of the transversal wave is approximated by the cylinder diameter D. Therewith, the average frequency of the transversal wave is calculated to $f = 1.57$ Hz. This frequency is approximately equal to the vortex shedding frequency $f_S = 1.68$ Hz at the critical Reynolds number. Therefore, the interaction of the vortices and the hairy flaps at this Re-number can be interpreted as lock-in of the vortex shedding frequency with the characteristic natural frequency of the traveling wave along the hairs at the aft of the body. Therefore, we approximated the fundamental frequency of the transversal wave by the vortex shedding frequency at $Re = 14\,750$ to $f_N^* = f_S = 1.68$ Hz.

Considering these observation we examine the vortex shedding in light of the cylinder-wake resonator model first proposed by Sigurdson and Roshko [16] to find an explanatory model for the jump in the *Str*–*Re*-plot (Fig. 8(b)). They postulated a resonance of instabilities in the separation bubble, which significantly influence the vortex shedding frequency (resonator model). Experiments on a two-dimensional step in a wind tunnel examined two independent kinds of instabilities which were related to fluctuations in the separated shear-layer and the vortex-shedding [15]. They argued that the vortex shedding frequency is not dictated by the shear-layer instabilities, but the resonance of instabilities in the separation bubble. Experimental investigations on periodically separating vortices showed a correlation between the kinematics of the vortices and the length of the separation bubble [15]. In detail, it is shown that the vortex-shedding frequency normalized with the length of the separation bubble and the free-stream flow velocity is nearly constant over a wide range of Reynolds

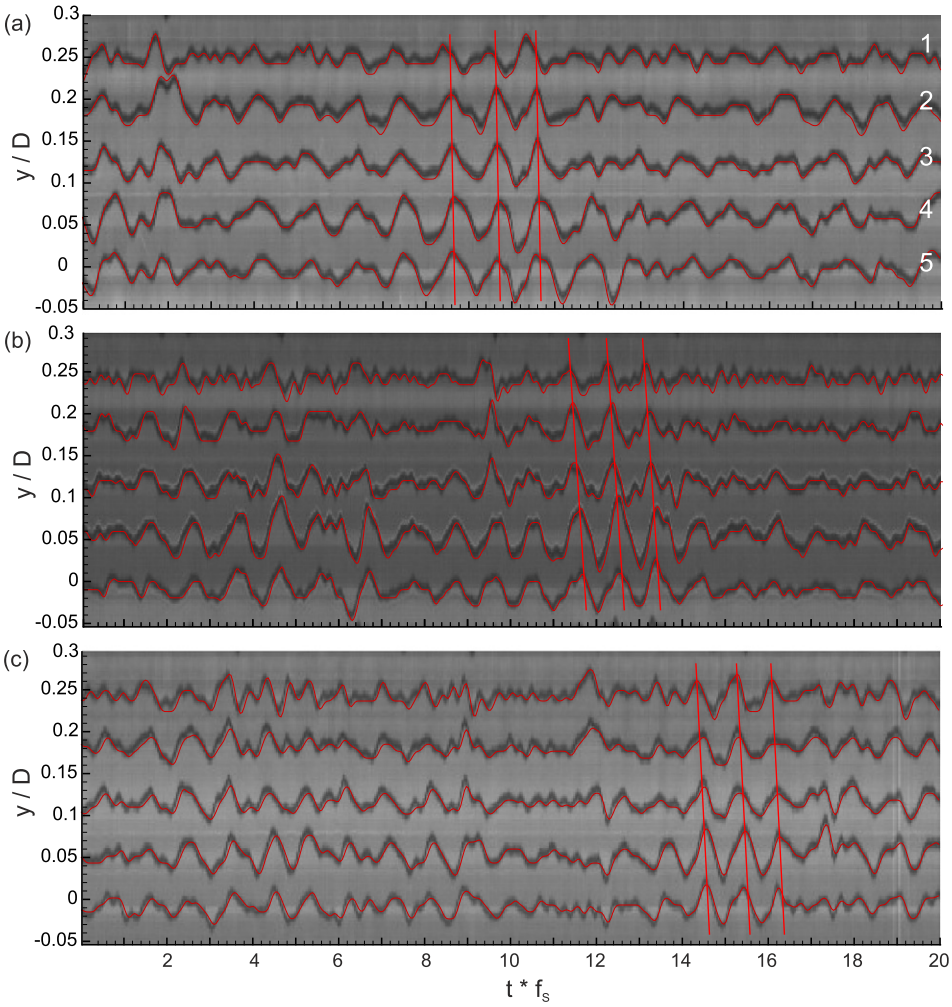

Fig. 10. Spatial-temporal reconstruction of the gray values along the red line in Fig. 9 with superimposed tracked positions of the hairy flaps tip ($(h/H = 1)$ for: (a) $Re = 12\,062$; (b) $Re = 14\,750$; (c) $Re = 20\,125$. The time scale is for all Re the same $t = 10$ s. The number of the hairy flaps as referred in the text are given in (a).

number [15]. Considering the differences of the separation before and after lock-in with the hair flap motion, we suggest that the classical formulation of the Strouhal number with the diameter of the cylinder as characteristic length scale is not suitable for the cases with hairy flaps, since the resonator is affected by the quasi-flexible wall conditions at the aft-part of the cylinder. Therefore, an adapted Strouhal number Str_{adapt} is calculated with x_0 as characteristic length scale equal to the length of the separation bubble. Fig. 12 shows the dependency of the adapted Str_{adapt} number from the Re number for the reference cylinder and both cases of hairy flaps ($h/H = 1$, $h/H = 0.1$). Comparing the plot of Str_{adapt} for the three cases, only small variations ($< 0.03 Str_{adapt}$) along Re and between the cases can be found. Thus, the flexible hairy flaps at the downstream-facing wall of the cylinders change the resonator in the way, that they decrease the resonator length after lock-in.

Another indication of the change of the shedding cycle after lock-in with the hairy flap motion is found from the analysis of the snapshot POD (Proper orthogonal decomposition) of the velocity and vorticity fields. The energy fraction of the velocity field is at maximum for the zeroth eigen-mode and its structure corresponds to that of the time averaged flow field. Since the focus of the investigations lied on the dynamic modes, the time averaged flow field was subtracted before the POD analysis to eliminate the influence of the mean flow. Fig. 13 shows the distribution of the energy fraction over the POD modes at (a) $Re = 12\,062$ and (b) $Re = 20\,125$ for the reference cylinder and the cylinder with hairy flaps ($h/H = 1$). At lower Re the difference between the two cases are only marginal, see Fig. 13(a).

At higher Re the energy fraction for the cylinder with hairy flaps is shifted towards mode #0 and mode #1, due to the influence of the hairy flaps on the vortex shedding (Fig. 13(b)). Therefore, the energy fraction of mode #2 is decreased by 63.9% based on the energy of mode #2 for the reference cylinder. This is a clear hint of a change in vortex shedding characteristics, according to the shift in the vortex shedding frequency at $Re \approx 14\,000$. Finally the distribution of the energy fraction a was used to reconstruct the flow field $U_r(x, y)$ for mode $i = 0, 1, 2$, according to Eq. (4).

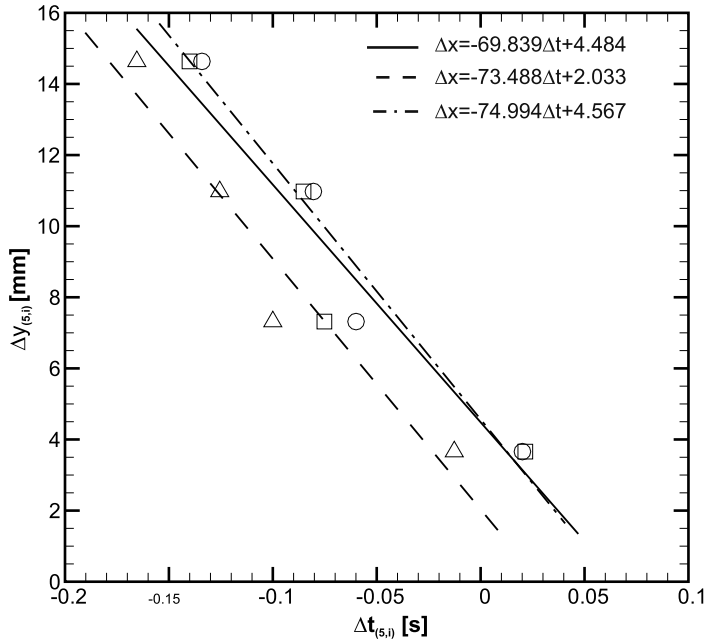

Fig. 11. Plot of the distance between ith and fifth hairy flap $\Delta y(i,5)$ and time shift of their motion $\Delta t(i,5)$ at: □ — $12t \cdot f_s$; △ --- $13t \cdot f_s$; ○ -·- $14t \cdot f_s$ for $Re = 14\,750$.

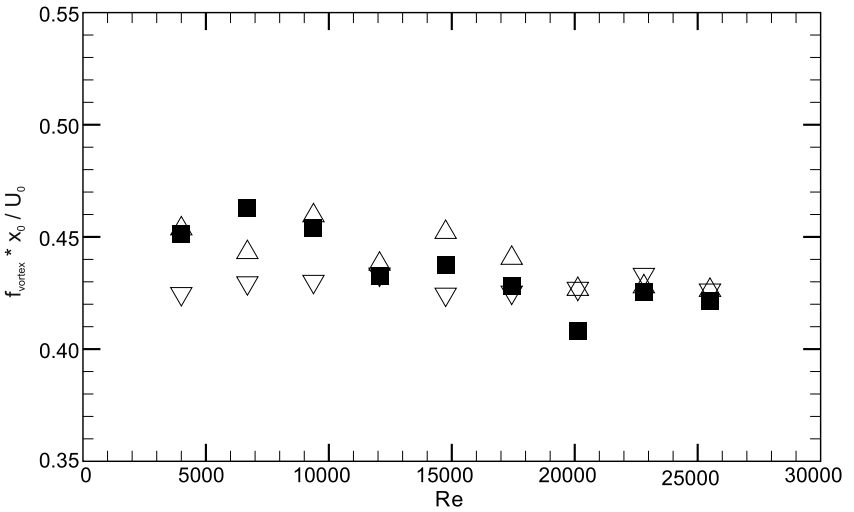

Fig. 12. Dependency of the adapted Strouhal number $f_S \cdot x_0/U_0$ from the Reynolds number Re for: ■ reference cylinder; △ cylinder with hairy flaps, $h/H = 1$; ▽ cylinder with hairy flaps, $h/H = 0.1$.

$$U_r(x, y) = \sum_{i=0}^{2} \left(a^i(t) \cdot \phi_{U^i(x,y)}\right) \tag{4}$$

Fig. 14 shows a contour-plot of the resulting spanwise vorticity $\omega_{z,r}$ at $Re = 12\,062$ for the reference cylinder and the case with hairy flaps ($h/H = 1$). The vorticity is given color-coded in a range of 20% of minimum $\omega_{z,r}$ (blue) and 20% of maximum $\omega_{z,r}$ (red) to identify the vortex cores with regions of concentrated vorticity. Furthermore, negative contour-lines are represented by dashed lines. Fig. 15 shows the reconstructed vorticity plots for $Re = 20\,125$. Keep in mind that the direction of rotation of the vortices in the POD modes is reversible due to the periodical character of the flow. Therefore, only their size, strength and distribution are important for the comparison of the two cases with and without hairy flaps. A first qualitative comparison of the reconstructed vorticity fields shows a significant influence of the motion of the hairy flaps on the flow when the lock-in effect is present (see the comparison at $Re = 20\,125$). The structure of the eigen-modes differs strongly from the case without hairy flaps affirming our suggestions of a changed vortex-shedding cycle. On the other hand, below the critical Reynolds number there are no significant differences between the two cases (compare the results

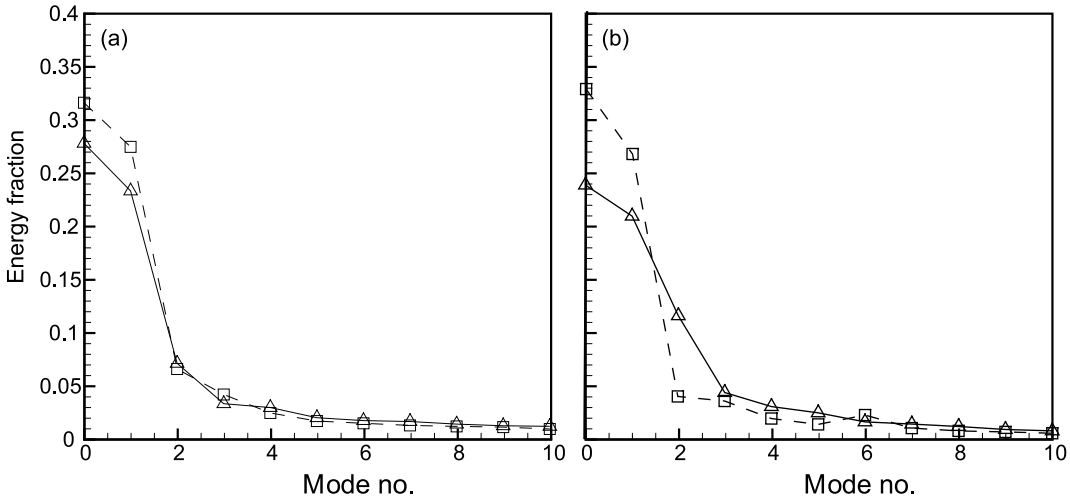

Fig. 13. Energy spectrum of the snapshot POD analysis for: (a) $Re = 12\,062$; (b) $Re = 20\,125$; –△– reference cylinder; --□-- cylinder with hairy flaps, $h/H) = 1$.

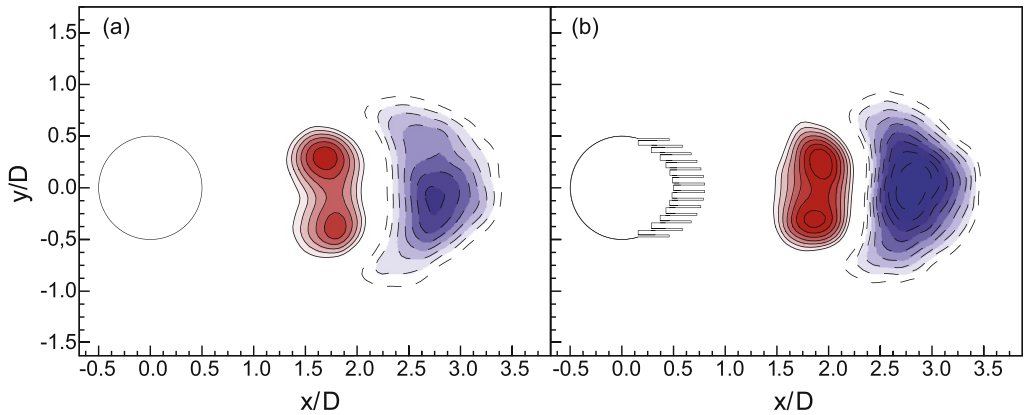

Fig. 14. Reconstruction of concentrated spanwise vorticity in the wake $\omega_{z,r}$ for the reference cylinder (a) and the cylinder with hairy flaps, $h/H = 1$ (b) corresponding to energy weighted sum of the zeros', first and second POD modes. The Reynolds number is $Re = 12\,062$. The vorticity contours are given in the range between red: 20% minimum $\omega_{z,r}$ and blue: 20% maximum $\omega_{z,r}$. Negative contour-lines are represented by the dashed lines. All values in the shadow region beneath the cylinder ($x/D < 0.5$, $y/D < 0$) are blanked out.

at a Reynolds number of $Re = 12\,062$). Furthermore, symmetric structures at the y-axis are visible for all cases. However, the distance between the two symmetric vortices for the case with hairy flap is reduced (Fig. 15(b)).

The results of the POD-analysis show that the transversal dislocation of the shed vortices away from the centerline is considerably reduced in case of the hairy flaps. As are result, the shed vortices are not arranged in a classical zig-zag pattern such as in the Kármán-vortex-street, rather they are arranged in a row along the centerline ($y = 0$). Fig. 16(a) and (b) illustrates the velocity vector fields with superimposed vorticity distributions for two time steps of the vortex shedding cycle. The vorticity is color-coded and given in the range between 20% minimum ω_z (blue) and 20% maximum ω_z (red).

A comparison of the two cases by means of the instantaneous velocity and vorticity field in Fig. 16 demonstrates that the arrangement of the vortices in the wake has been changed. In the reference case, the induced flow between two successive vortices has a large backflow component (Fig. 16(c)), which means also a large wake deficit in the axial velocity profile and therefore a large drag force acting on the cylinder. In contrast, with hairy flaps the wake deficit is largely reduced in comparison to the reference case and therefore the drag force acting on the cylinder is reduced, too (Fig. 16(d)). Fig. 17 illustrates the correlations between the flow fluctuations in the separation bubble ($\mathrm{rms}(U_x)_{rel}$ (a), $\mathrm{rms}(U_y)_{rel}$ (b)) and the frequency ratio f_0^*/f_S. For ratios smaller than 1, the vortex shedding is in lock-in mode with the hairy flaps. On the other hand, a ratio larger than 1 indicates that the shedding frequency is not high enough to match the conditions for excitation of the traveling wave. A rough estimate of the drag force is calculated from the axial momentum balance (comparing $X/D = -2$ and $x/D = 2$) according to Eq. (5).

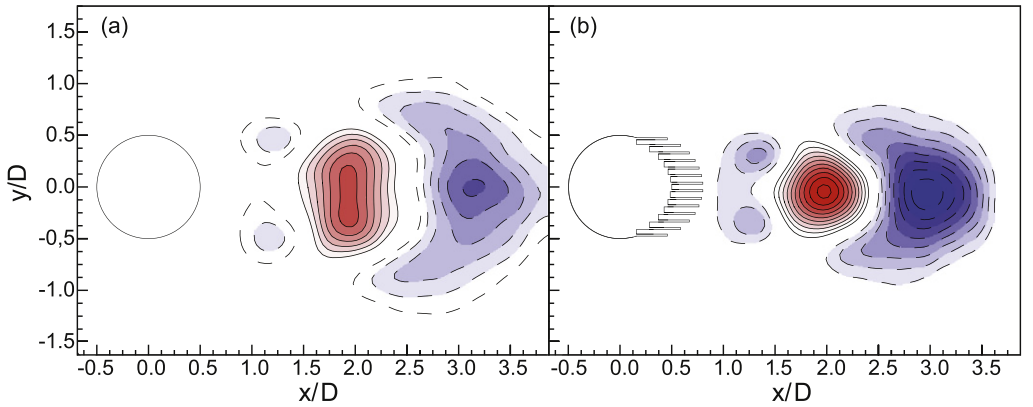

Fig. 15. Reconstruction of concentrated spanwise vorticity in the wake $\omega_{z,r}$ for the reference cylinder (a) and the cylinder with hairy flaps, $h/H = 1$ (b) corresponding to energy weighted sum of the zeros', first and second POD modes. The Reynolds number is $Re = 20\,125$. The vorticity contours are given in the range between red: 20% minimum $\omega_{z,r}$ and blue: 20% maximum $\omega_{z,r}$. Negative contour-lines are represented by the dashed lines. All values in the shadow region beneath the cylinder ($x/D < 0.5$, $y/D < 0$) are blanked out.

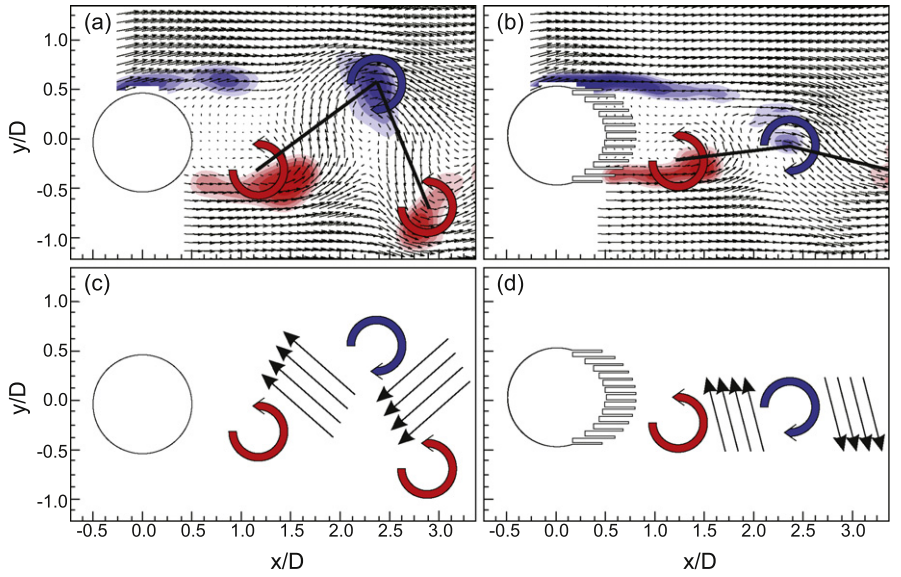

Fig. 16. Illustration of the influence of the hairy flaps on the shed vortex location in the wake for $Re > 14\,750$ for one instant of the vortex shedding cycle: (a, c) reference cylinder; (b, d) cylinder with hairy flaps, $h/H = 1$. Only every second vector is displayed in both directions and the color represents the spanwise vorticity ω_z in the range between 20% minimum ω_z blue and 20% maximum ω_z blue. Vectors in the shadow region beneath the cylinder ($x/D < 0.5$, $y/D < 0$) are blanked out. The direction of rotation of the vortices is indicated by the colored arrows. The arrows in (c) and (d) correspond to the assumed directions of the induced velocities.

$$\Delta I_x = \rho \cdot \left[\int_{-1.5D}^{1.5D} U_x(x/D = -2)^2 \,\mathrm{d}y - \int_{-1.5D}^{1.5D} U_x(x/D = 2)^2 \,\mathrm{d}y \right] \tag{5}$$

The rms-values and the drag force are normalized with the results of the reference cylinder without flaps. Therefore, values smaller 100% correspond to a reduction of flow fluctuation in the wake-flow or correspondingly a reduction of drag force. As expected, the global maximum of $\mathrm{rms}(U_y)_{rel}$ appears at a frequency ratio of $f_0^*/f_S = 1$ where the flap motion is in resonance with the vortex shedding frequency and the amplitude is maximum. For smaller frequency ratios $f_0^*/f_S < 1$ the traveling wave motion is in lock-in mode. The general trend in Fig. 17(a) and (b) is similar to the results of [2]. In the lock-in range, flow fluctuations are reduced by 42% in x- and 35% in y-direction at best (Fig. 17(a), (b)). In addition, the drag forces are roughly at 95% that of the reference cylinder (Fig. 17(c)). In addition, it follows from conservation of momentum that the reduced rms fluctuations of the velocities in the wake are synonymous to reduced rms fluctuation of the forces acting on the cylinder. Therefore, the hairy flaps not only reduce the mean drag but the rms values of force fluctuations as well. This result holds for the drag and the lift force.

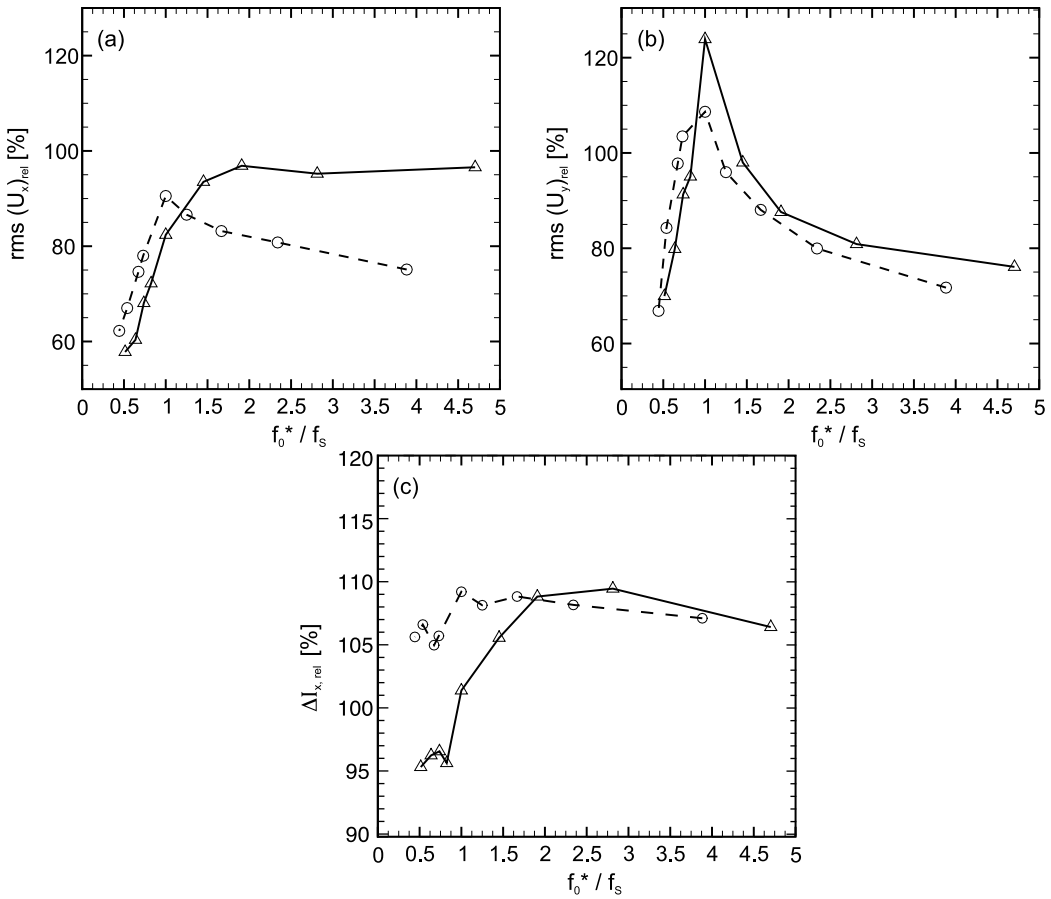

Fig. 17. Trends for varying frequency ratio f_0^*/f_S of: (a) flow fluctuations in streamwise x-direction $\mathrm{rms}(U_x)_{rel}$; (b) flow fluctuations in transversal y-direction $\mathrm{rms}(U_y)_{rel}$; (c) axial momentum balance ΔI_x. The flow fluctuations and the values of $\Delta I_{x,rel}$ are normalized with the reference case of a cylinder without hairy flaps and the results are given for: –△– hairy flaps $h/H = 1$ and --○-- $h/H = 0.1$.

4. Conclusion

The influence of flexible, self-adaptive hairy-flaps on the dynamics of a cylinder wake flow is investigated experimentally. The basic principle is inspired by the numerical studies of [2] on a hairy-coating as a concept of passive flow control. Therefore a cylinder was generated by stacking circular segments where flexible hairy-flaps extend from the aft part downstream into the wake region. A total number of 14 flaps were distributed homogeneously along the semi-circular aft part of the segments facing in downstream direction. At first the mechanical properties of a single hairy-flap and the influence of neighboring hairy-flaps in the bundle were characterized. Thereafter, the velocity field around a cylinder without and with hairy-flaps was measured by particle image velocimetry in a range of $5000 < Re < 31\,000$. Furthermore, the motions of the hairy-flaps were recorded simultaneously.

A major result of the flow studies is the characteristic jump in the *Str*–*Re*-plot at a critical Reynolds number of $Re_c \approx 14\,000$ towards higher Strouhal numbers compared to the classical behavior of cylinder wake flow. The analysis of the motions of the hairy-flaps shows that for $Re = Re_c$ the amplitude of the flap motion is considerably increased, hinting on a resonant excitation. In addition, the wake flow shows the highest rms-values of the transversal velocity component in the wake region. Beyond Re_c neighboring hairy-flaps start to move more regular and in the same motion pattern with a small but distinct phase shift. Thus, a traveling wave is generated in the flexible flap bundle which propagates in transversal direction along the hair rows. The consequence of this flow–structure interaction is that: (i) the length of the separation bubble behind the cylinder is decreased; (ii) vortex shedding frequency is increased; and (iii) rms-values of the velocity components in x- and y-directions within the wake region are decreased. Furthermore, the POD results of the wake velocity and vorticity fields show, that the energy fraction of the first and second eigen-values are decreased due to the influence of the flaps at $Re > Re_c$. The reconstruction of the velocity vector fields for the first three eigen-modes show, that the hairy-flaps alter the vortex shedding in such a way that the transversal dislocation (transversal distance from the centerline) of the shed vortices is largely reduced. Accordingly, the vortices are not arranged in a classical zig-zag pattern of the Kármán-vortex-street, rather they are shed in a row along the centerline ($y = 0$). As a consequence, the momentum loss (wake deficit) and the forces acting on the cylinder are reduced.

The jump in the Strouhal number for increasing Reynolds number appears just at the moment, where the vortex shedding period matches with the characteristic period of the traveling wave through the hairy-flap bundle along the semi-circular aft-part of the cylinder. This resembles the occurrence of a lock-in effect in wake dynamics around flexible bluff bodies (e.g. [17]). Accordingly, the natural frequency of the transversal-wave f_0^* is given by the vortex shedding frequency f_S at the jump of the Strouhal number. Such a transversal wave mechanism along the flexible hairs at the aft part of the cylinder also alter the boundary conditions of the resonator model proposed by [15] to describe the natural frequency of vortex shedding behind bluff bodies. Propagating waves within the separation bubble see a different situation when interacting with a semi-flexible and permeable boundary imposed by the flexible hair bundle in comparison to a solid surface at the aft part of the cylinder. When we take in our results the characteristic length-scale for the wake dynamics as the streamwise length of the separation bubble, the *Str–Re* profile is again regular without any jump. This indicates, that the dominant instabilities for the vortex shedding process are originating from the separation bubble rather than from the shear layer roll-up process. As a conclusion, the jump in shedding frequency at Re_c can be explained as a resonance mode change of the separation bubble where the hairy-flap bundle imposes a new boundary condition as a flexible wall with visco-elastic coupling in transversal direction.

Combing the results of the PIV measurements with the motion analysis it is found that, flow fluctuations are reduced by 42% in x- and 35% in y-direction for a frequency ratio of $f_0^*/f_S \approx 0.5$, compared to a reference case without hairy-flap. In conclusion, we show that for an optimum flow control the mechanical properties of this kind of hairy-flaps should result in a frequency ratio smaller than 1, compared to $f_0^*/f_S \approx 3$ as suggested by [2] for a hairy-coating. This discrepancy between the results of [2] on hairy-coating and the results presented herein on hairy flaps can be explained by the differences in the mechanical parameters of the hairy flaps and the much higher *Re* number of the experimental investigations.

Appendix A

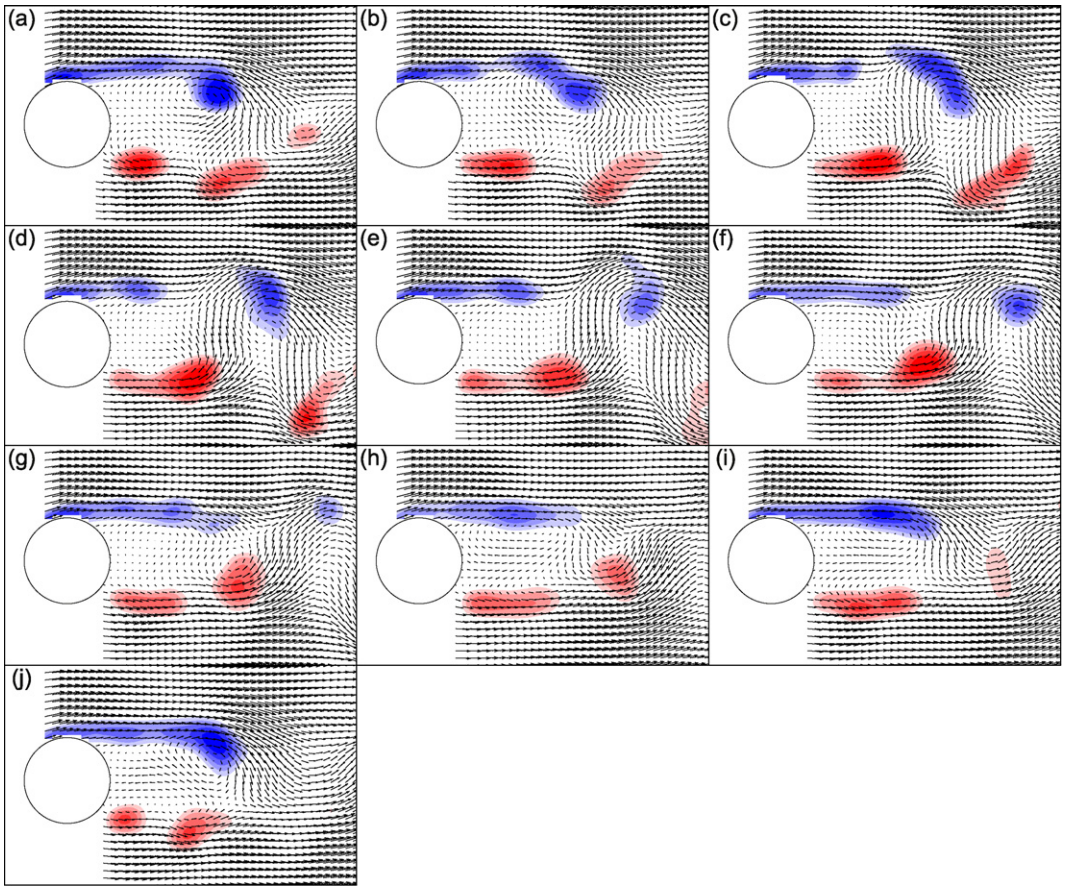

Fig. A.18. Time series of ten subsequent vector plots for one period of the vortex shedding at the reference cylinder without hairy flaps. The Reynolds number is $Re = 20\,125$. Every second vector in both directions is skipped and the color represents the vorticity ω_z in the range between 20% minimum ω_z blue and 20% maximum ω_z red.

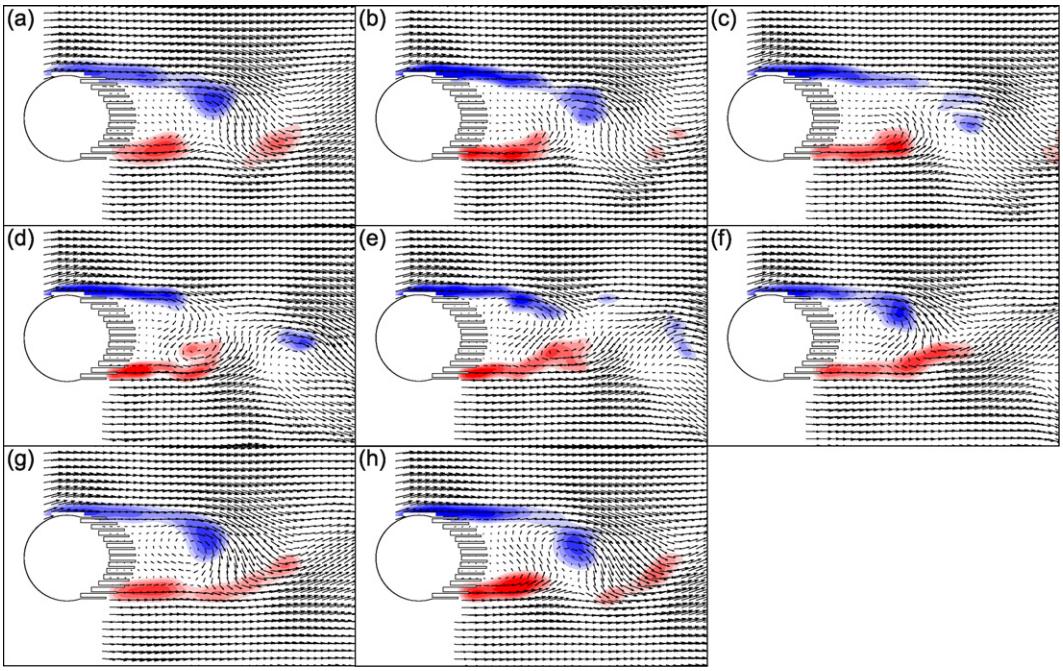

Fig. A.19. Time series of ten subsequent vector plots for one period of the vortex shedding at the cylinder with hairy flaps $h/H = 1$. The Reynolds number is $Re = 20\,125$. Every second vector in both directions is skipped and the color represents the vorticity ω_z in the range between 20% minimum ω_z blue and 20% maximum ω_z red.

References

[1] C.H.K. Williamson, Vortex dynamics in the cylinder wake, Annu. Rev. Fluid Mechanics 28 (1996) 477–539.
[2] J. Favier, A. Dauptain, D. Basso, A. Bottaro, Passive separation control using a self-adaptive hairy coating, Journal of Fluid Mechanics 627 (2009) 451–483.
[3] J.C. Owen, A.A. Szewczyk, P.W. Bearman, Suppressing Karman vortex shedding by use of sinuous circular cylinders, Bulletin of the American Physical Society 44 (1999) 124.
[4] J.C. Owen, A.A. Szewczyk, P.W. Bearman, Suppression of Karman vortex shedding, Gallery of Fluid Motion Physics of Fluids 12 (2000) 1–13.
[5] J.C. Owen, P.W. Bearman, Passive control of VIV with drag reduction, Journal of Fluids and Structures 15 (3–4) (2001) 597–605.
[6] W. Hanke, M. Witte, L. Miersch, M. Brede, J. Oeffner, M. Michael, F. Hanke, A. Leder, G. Dehnhardt, Harbor seal vibrissa morphology suppresses vortex induced vibrations, Journal for Experimental Biology 213 (2010) 2665–2672.
[7] H.H. Nigim, S.M. Batill, Flow about cylinders with surface perturbations, Journal of Fluids and Structures 11 (8) (1997) 893–907.
[8] A.E. Perry, W.H. Schofield, P.N. Joubert, Rough wall turbulent boundary layers, Journal of Fluid Mechanics 37 (1969) 383–413.
[9] P.W. Bearman, Investigation of flow behind a 2-dimensional model with A blunt trailing edge and fitted with splitter plates, Journal of Fluid Mechanics 21 (1965) 241–255.
[10] K. Kwon, H. Choi, Control of laminar vortex shedding behind a circular cylinder using splitter plates, Physics of Fluids 8 (1996) 479–486.
[11] H. Akilli, C. Karakus, A. Akar, B. Sahin, N.F. Tumen, Control of vortex shedding of circular cylinder in shallow water flow using an attached splitter plate, Journal of Fluids Engineering – Transactions 130 (4) (2008) 041401.
[12] S. Shukla, R. Govardhan, J.H. Arakeri, Flow over a cylinder with a hinged-splitter plate, Journal of Fluids and Structures 25 (4) (2009) 713–720.
[13] A. Dauptain, J. Favier, A. Bottaro, Hydrodynamics of ciliary propulsion, Journal of Fluids and Structures 24 (8) (2008) 1156–1165.
[14] Ch. Brücker, A. Keissner, Streaming and mixing induced by a bundle of ciliary vibrating micro-pillars, Exp. in Fluids 46 (1) (2010) 57–65.
[15] A. Boiko, G.R. Grek, A. Dovgal, V. Kozlow, The Origin of Turbulence in Near-Wall Flows, Springer, Berlin, 2002.
[16] L. Sigurdson, A. Roshko, The structure and control of a turbulent reattaching flow, Turbulent Management and Relaminarization (1988) 497–514.
[17] C.H.K. Williamson, R. Govardhan, Vortex-induced vibrations, Annu. Rev. Fluid Mech. 36 (2004) 413–455.